On The Multiscale Structure and Morphology of PVDF-HFP@MOF Membranes in The Scope of Water Remediation Applications

Ainara Valverde,* Roberto de Fernandez-de Luis,* Hugo Salazar, Bruna F. Gonçalves, Stephen King, László Almásy, Manfred Kriechbaum, José M. Laza, José L. Vilas-Vilela, Pedro M. Martins, Senentxu Lanceros-Mendez, José M. Porro, and Viktor I. Petrenko

Poly(vinylidene fluoride-co-hexafluoropropylene) (PVDF-HFP) is a highly versatile polymer used for water remediation due to its chemical robustness and processability. By incorporating metal-organic frameworks (MOFs) into PVDF-HFP membranes, the material can gain metal-adsorption properties. It is well known that the effectiveness of these composites removing heavy metals depends on the MOF's chemical encoding and the extent of encapsulation within the polymer. In this study, it is examined how the micro to nanoscale structure of PVDF-HFP@MOF membranes influences their adsorption performance for Cr^{VI}. To this end, the micro- and nanostructure of PVDF-HFP@MOF membranes are thoroughly studied by a set of complementary techniques. In particular, small-angle X-ray and neutron scattering allow to precisely describe the nanostructure of the polymer-MOF complex systems, while scanning microscopy and mercury porosimetry give a clear insight into the macro and mesoporosity of the system. By correlating nanoscale structural features with the adsorption capacity of the MOF nanoparticles, different degrees of full encapsulation-based on the PVDF-HFP processing and structuration from the macro to nanometer scale are observed. Additionally, the in situ functionalization of MOF nanoparticles with cysteine is investigated to enhance their adsorption toward Hg^{II}. This functionalization enhanced the adsorption capacity of the MOFs from 8 to 30 mg·g^{-1}.

1. Introduction

Water pollution has become an increasingly alarming global issue. Of the various emerging pollutants, heavy metals have garnered significant concern due to their toxicity, teratogenicity, and carcirogenicity.[1] Among the different strategies to capture heavy metal ions from water, adsorption holds considerable promise due to its simplicity and cost efficiency. However, classic sorbents suffer from low adsorption capacity[2] and selectivity due to their limited chemical tailorability.

Here, Metal-Organic Frameworks (MOFs) are becoming an interesting family of porous materials to face this problem. MOFs are crystalline solids built from metal ions or clusters connected by organic linkers to form extended, ordered, and highly porous networks.[3–7] Given these propertied, MOFs stand out as alternative technologies for water remediation purposes thanks to their ordered porosity metrics

A. Valverde, R. de Fernandez-de Luis, H. Salazar, B. F. Gonçalves, S. Lanceros-Mendez, J. M. Porro, V. I. Petrenko
BCMaterials
Basque Center for Materials
Applications and Nanostructures
UPV/EHU Science Park, Leioa 48940, Spain
E-mail: ainara.valverde@bcmaterials.net; roberto.fernandez@bcmaterials.net

A. Valverde, J. M. Laza, J. L. Vilas-Vilela
Macromolecular Chemistry Group (LABQUIMAC)
Department of Physical Chemistry Faculty of Science and Technology
University of the Basque Country (UPV/EHU)
Barrio Sarriena s/n 48940 Leioa, Spain, Bilbao 48013, Spain

S. King
ISIS Neutron and Muon Facility
Science & Technology Facilities Council
Rutherford Appleton Laboratory
Didcot OX11 0QX, UK

L. Almásy
Institute for Energy Security and Environmental Safety
Centre for Energy Research
Budapest 1121, Hungary

M. Kriechbaum
Institute of Inorganic Chemistry
Graz University of Technology
Graz 8010, Austria

(i.e., record surface area, tunable pore volume/window...) and their versatility to be encoded with functionalities placed surgically at specific positions of their frameworks.[8–14] Among the various MOFs reported up to date, the Zr and Ti-based MOFs as MOF-808 $(Zr_6O_4(OH)_4(C_9H_6O_6)_2(HCOO)_6)$, UiO-66-NH$_2$ $(Zr_6O_4(OH)_4(C_8H_7NO_4))$, and MIL-125 $(Ti_8O_8(OH)_4(C_8H_6O_4)_6)$ are among the most applied ones for these purposes.

Nevertheless, the practical application of MOFs in real-life experiments is hindered by their powdered nature, which poses challenges in terms of time and energy consumption during the recovery process from water. As a consequence, the immobilization of these active sorbents with mechanically robust polymeric matrixes stands out as one of the most appealing strategies to solve this handicap.

Poly(vinylidene fluoride-co-hexafluoropropylene) (PVDF-HFP), is a chemically, thermally, and mechanically robust polymer widely employed for water remediation purposes.[15] One of the main advantages of PVDF-HFP is its easy and widely-studied processability.[16–26] This opens the perspective to shape it as water-filters and membranes with tailored porous structures.[27–31]

However, the permeability and adsorbing capacity of these membranes are limited because of their hydrophobicity. The integration of nanomaterials, and in particular of MOFs, into the polymeric porous structure of the PVDF-HFP represents a suitable strategy to improve the overall properties and functionality of the membranes based on this per-fluorinated polymer.[32,33]

Among the different processing routes to prepare composites based on PVDF-HFP, phase separation is one of the most appropriate to obtain membranes with a well-interconnected porosity network suitable for water remediation. It involves the transition from a solution of the polymer in an organic solvent to the porous interconnected membranes based on PVDF-HFP. The process can be achieved by different routes such as: thermally induced phase separation (TIPS), non-solvent induced phase separation (NIPS), vapor-induced phase separation (VIPS), and evaporation-induced phase separation (EIPS).[24,34,35] The type and conditions of the phase separation process greatly influence the PVDF-HFP macro to nano-meter pores structures, as well as the homogeneous integration of the MOF nanomaterials into the PVDF-HFP matrix. That is, the processing of the PVDF-HFP is key to i) avoiding the complete encapsulation of the MOFs, ii) enhancing their surface exposure into the interconnected pore-space of the polymeric matrix, and iii) preventing their detachment during working conditions.[36]

Overall, these characteristics are closely related to the multiscale structuration of the composites from the nano- to the macroscale. Even if PVDF-HFP composites have been profoundly studied from the macro to the microscopic regimes, the investigations aiming to uncover the nanostructure of these composites mainly via small-angle scattering techniques (i.e., small-angle X-ray (SAXS) and neutron (SANS) scattering) are still limited.[37,38] This issue is nevertheless essential for improving membranes functional response, since SAXS and SANS can give access to critical aspects such as i) the distribution of the MOF particles into the PVDF-HFP polymer matrix, ii) the interconnection of their pore-space, or iii) the interface between the MOF and the PVDF components.[39,40] In addition, all these features may have a significant impact on the functionality of the composite membranes to capture target pollutants from water.

In this work, the templating effect of MOF nanoparticles (MOF-808, UiO-66-NH$_2$, and MIL-125) into the porous structure of PVDF-HFP@MOF composites processed by TIPS and NIPS has been investigated by means of X-ray diffraction (XRD), infrared spectroscopy (IR), thermogravimetric analysis (TGA), and scanning electron microscopy (SEM). As a first step, the main physicochemical properties of such composites were analyzed. Them, the macro, meso, and microporous structure of the composites have been characterized by a combination of specific experimental techniques, including mercury porosimetry, SEM, SAXS, and SANS. Altogether, a complete landscape from the macro to the nanometer scale of the structure of the composites has been obtained and correlated with the encapsulation degree of the MOF nanoparticles into the polymeric matrix, and hence to their capacity to capture chromate oxyanions (CrO_4^{2-}). We have demonstrated as well that the MOFs included within the membranes can be i) directly functionalized with cysteine via solvent-assisted ligand incorporation (SALI) to adapt its adsorption affinity toward the capture of soft metal ions as Hg^{II}, and ii) that the efficiency of their SALI functionalization of the MOFs within the membrane depends as well on their encapsulation degree. All in all, this fundamental understanding of the system opens the room to identify the best processing protocols to develop PVDF-HFP@MOF composite membranes applied for water remediation purposes.

2. Results and Discussion

2.1. Sorbents Characterization

Metal-Organic Frameworks were selected due to their i) good water stability, ii) affinity toward the adsorption of metal oxyanions, and iii) chemical taylorability to modulate their adsorption properties. Once synthesized, solvent exchanged and activated, a full characterization of the MOFs and PVDF-HFP@MOF membranes was performed by XRD, IR, CO$_2$ adsorption, and TGA. The visual comparison between the MOFs' experimental and simulated XRD patterns reveals a full agreement among them (Figure 1a–c). As expected, a slight broadening of the diffraction maxima is observed due to their nanometer-scale size, especially for MOF-808 and UiO-66-NH$_2$. As confirmed by SEM, UiO-66-NH$_2$ (50–100 nm), and MOF-808 (150–200 nm) show a smaller particle diameter in comparison to the one of MIL-125 (100–500 nm) (Figure 1d–f). It is worth pointing out that a large

P. M. Martins
Centre of Molecular and Environmental Biology (CBMA)
University of Minho
Braga 4710-057, Portugal

P. M. Martins
Institute for Research and Innovation on Bio-Sustainability (IB-S)
University of Minho
Braga 4710-057, Portugal

S. Lanceros-Mendez, J. M. Porro, V. I. Petrenko
IKERBASQUE
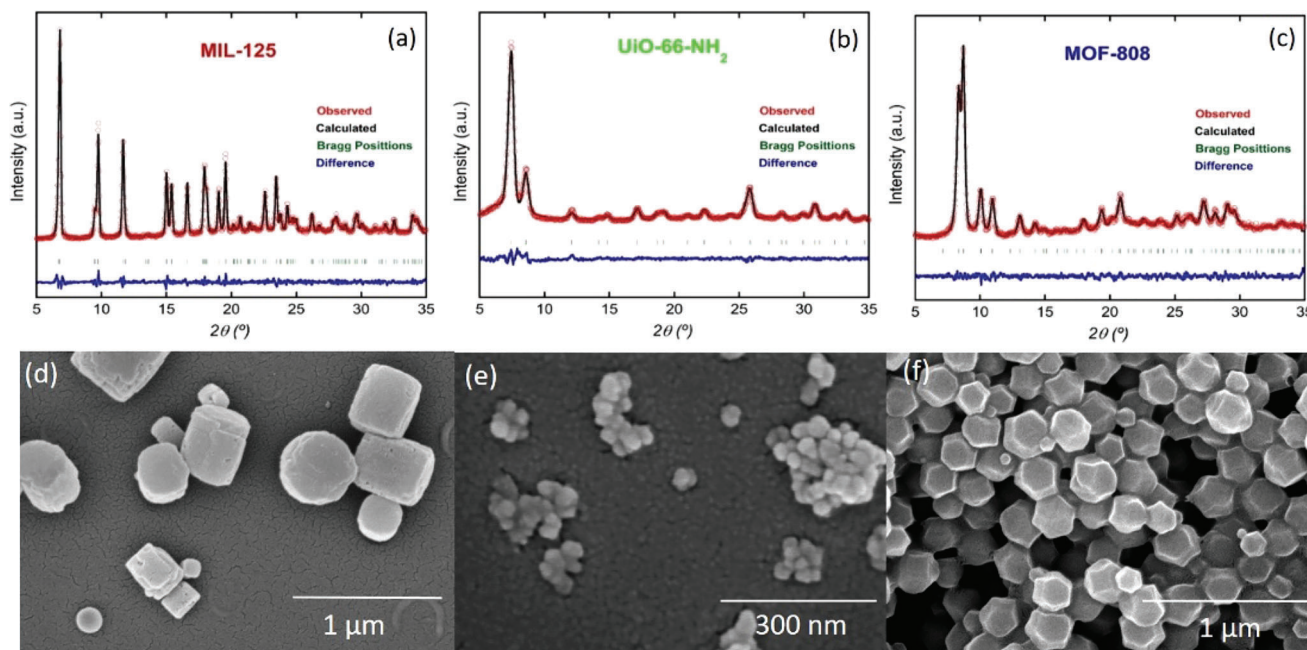Basque Foundation for Science
Bilbao 48009, Spain

Figure 1. a–c) Full profile matching analysis of the XRD patterns of the MOF samples and d,e) SEM images of d) MIL-125, e) UiO-66-NH_2, and f) MOF-808.

agglomeration of the UiO-66-NH_2 particles has been observed by SEM and that among all the samples, MIL-125 is the most heterogeneous material in terms of particle size distribution and morphology. Thermogravimetric curves of the three MOFs (Figure S1a, Supporting Information) are similar to the ones reported in previous studies,[12,41] showing the thermal loss of solvent molecules (30 – 120 °C), coordinated species (120 – 350 °C), and the calcination of the organic linkers (350 – 600 °C). In addition, the type I CO_2 adsorption isotherms (Figure S1b, Supporting Information) confirm the microporous nature of the compounds (MIL-125[42] = 785 m^2 g^{-1}, UiO-66-NH_2[43] = 922 m^2 g^{-1}, and MOF-808[44] = 1037 m^2 g^{-1}).

2.2. Macro to Microporous Structure of PVDF-HFP@MOF Composites

The presence of the MOF in the PVDF-HFP composites was confirmed by IR (Figure 2a; Figure S2a, Supporting Information) and XRD (Figure 2c; Figure S2c, Supporting Information). Infrared spectra indicate that PVDF-HFP@MOF membranes crystallize in a mixture of both α and β phases. The bands corresponding to the β phase are found at 1234 and 840 cm^{-1}, while the ones of the α phase are located at 976 and 763 cm^{-1}.[45] It is not clear if the composites have a minor content of the γ-PVDF phase, as its characteristic signal (833 cm^{-1}) is located next to the one corresponding to the β phase.[45,46] The inclusion of the MOFs slightly modifies the crystallization phase of the TIPS membranes, with a slight increase of the band's intensity at 763 cm^{-1}, which is associated with the α-PVDF-HFP. XRD patterns of the composites confirm the presence of MOFs in the PVDF-HFP-based composites (Figure 2c; Figure S2c, Supporting Information). The characteristic diffraction maxima of the MOFs can be recognized in the

XRD patterns of all membranes. It is important to note that even if the MOF loading is the same for NIPS and TIPS membranes, the intensities of the diffraction peaks associated with the MOFs are quite different. A possible explanation is the presence of a heterogeneous distribution of the MOF in the polymer, as the TIPS membranes seem to have a higher density of MOF particles near the surface. The processing method also induces a change in the XRD signal coming from the polymeric matrix. Both membranes present the diffraction maxima expected for the α-PVDF-HFP, but composites processed by TIPS present narrower diffraction maxima and, therefore, a higher crystallinity in comparison to their homologue NIPS.

The thermal collapse of the PVDF-HFP matrix consists of two overlapped weight losses from 425 to 450 °C and 450 to 600 °C. These weight losses are related to carbon-hydrogen and carbon-fluoride bond scissions and occur in two partially overlapped steps due to the difference in the bond strength of C—H compared with C—F (410 and 460 kJ mol^{-1}, respectively) (Figure 2b; Figure S2b, Supporting Information).[36,47–49] MOF particles reduce the degradation temperature and the percentage of weight loss associated with the initial step, ascribed to the polymer's thermal collapse. This trend has also been reported for PVDF composites, including other inorganic and organic fillers.[45,50,51] In line with the thermogravimetric analyses, the DSC measurements of the PVDF-HFP and PVDF-HFP@MOF samples (Figure 2d; Figure S2d, Supporting Information) exhibit characteristic endothermic peaks that correspond to the melting temperature of the polymer (≈140 °C), but also to an endothermic process (60–90 °C) related to the dehydration of the MOFs. On the other hand, during cooling, the crystallization of the polymer is detected by the peak at ≈100 °C.

As revealed by SEM, TIPS processing leads to PVDF-HFP-composites with a slightly heterogeneous structure composed of

**ADVANCED
SCIENCE NEWS**

www.advancedsciencenews.com

**ADVANCED
MATERIALS
INTERFACES**
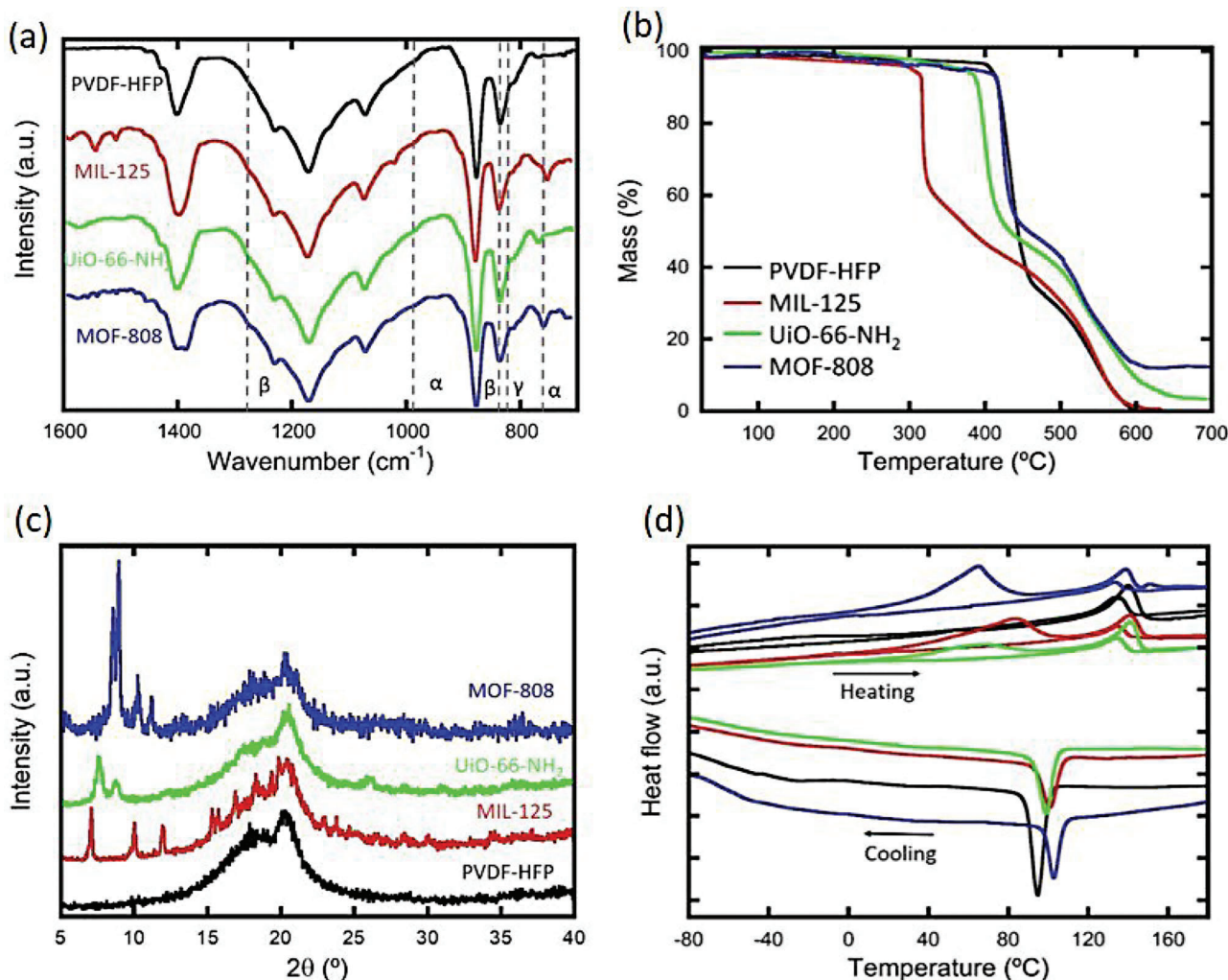Open Access

www.advmatinterfaces.de

Figure 2. a) FTIR spectra, b) thermogravimetric analysis, c) X-ray diffraction patterns, and d) differential scanning calorimetry for neat PVDF-HFP and PVDF-HFP@MOF composites processed by TIPS method.

interconnected macro-pores. This structuration is similar both in the cross section and at the surface of the membranes (Figure **3**). The surface of the composites shows a heterogeneous pore distribution ranging from 5 to 10 µm, suggesting a highly accessible interphase for the pollutants' migration into the membrane. The inclusion of MOF particles into the PVDF-HFP porous matrix slightly alters the geometry and pore size of the membrane at its surface and inner structure. Moreover, depending on the MOF integrated within the polymer, there are different changes in the morphology. The inclusion of MIL-125 induces a homogenization of the PVDF-HFP inner structure while it slightly increases the average pore size of the PVDF-HFP structure up to a size of ≈10 µm. In contrast, the porosity on the surface of the composite is significantly reduced in comparison to the one of the bare PVDF-HFP. For TIPS processed PVDF-HFP@UiO-66-NH$_2$, the main diameter of the pores at the inner structure and the surface of the composite is slightly reduced. Still, in general terms, a well-interconnected pores network is maintained. Finally, the inclusion of MOF-808 is the one that alters most of the porosity. On the one hand, the size of the pores at the surface is maintained,

but they show a heterogeneous distribution that leads to the generation of highly-porous and non-porous domains. Besides, the inner pores are significantly elongated and better defined than in the pristine PVDF-HFP membrane. The macropores at the body of the membrane show an average size of ≈10 µm, but narrower windows interconnect them. In addition, the MOF-808 particles are homogeneously placed, decorating the inner surface of the macropores. In the case of MIL-125 or UiO-66-NH$_2$-based composites, in addition to MOF particles located at the surface of the membrane, agglomerates of MOFs have also been detected within the pores of the PVDF-HFP matrix.

On the other hand, NIPS generates PVDF-HFP@MOF membranes with anisotropic structure and pore distributions (Figure S3, Supporting Information). Larger pores ≈10 µm in diameter appear near the surface of the composite. In contrast, smaller, anisotropic, and elongated pores of ≈2–3 µm in diameter are generated in the bulk of the membrane. In addition, the surface of the NIPS membrane exhibits a thin layer with a compact structure with isolated pores. It is essential to point out that the diameter of the pores generated within this thin layer is considerably
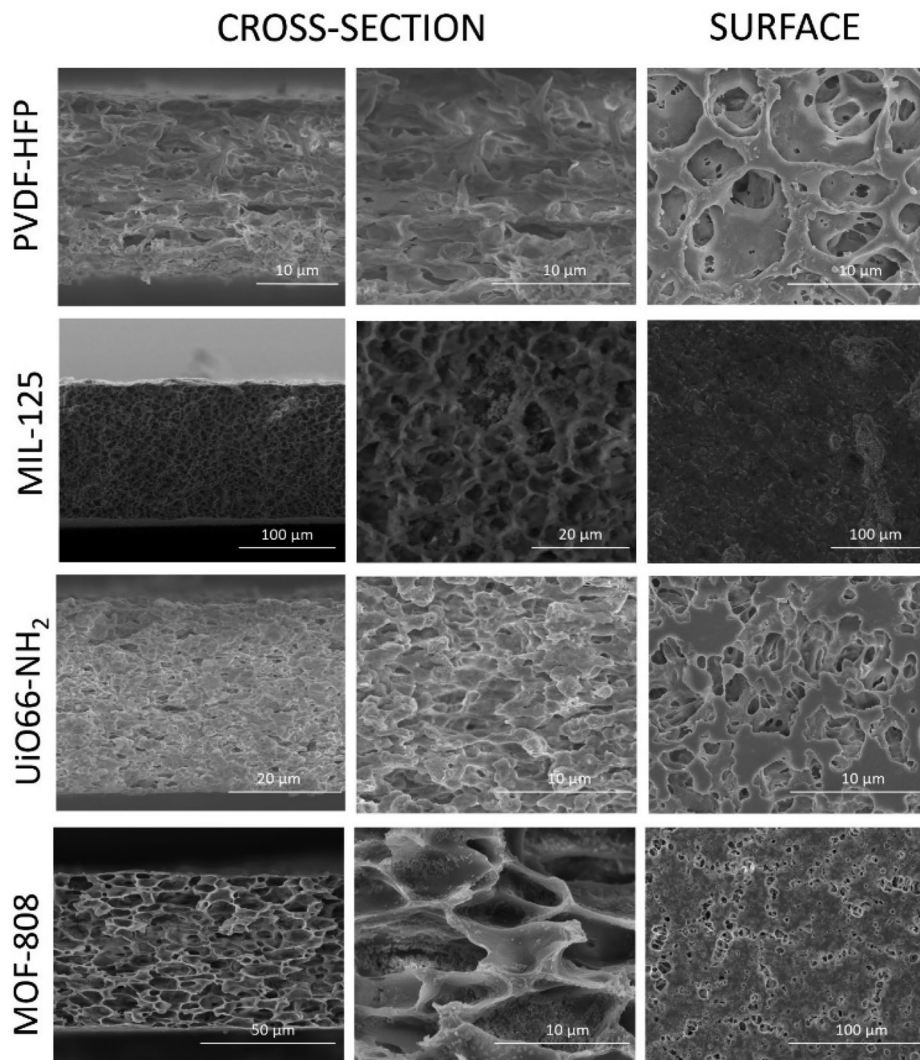
Figure 3. Representative SEM images prepared by TIPS.

smaller (i.e., 300 nm) than the one observed for their homolog TIPS membranes. In addition, the pores are isolated from each other. The structure of the thin film at the surface of the membrane is generally maintained when the MOFs are incorporated into the polymer, except for MOF-808, where its insertion causes a heterogenization of the pores' size and density. In addition, the MOF particles also modulate the anisotropic structuration within the body of the NIPS membranes so their incorporation makes the structure more homogeneous by preventing the formation of the larger macro-pores, usually located closer to the surface of the pure PVDF-HFP NIPS membrane.

The structure of the PVDF-HFP@MOF composites was further investigated by means of mercury porosimetry (Figure 4). PVDF-HFP TIPS membranes accumulate most of the volume of their accessible pores in those 1.5 µm diameter wide. In contrast with the main pore size observed in the SEM images (≈10 µm diameter), mercury porosimetry indicates that most of the surface area of the membrane lies within the pores with a smaller diameter of ≈1 µm. A similar trend is found for the composites based on MIL-125 and MOF-808, with most of the accessible volume lo-

cated at 1–1.5 µm diameter pores. In contrast, PVDF-HFP@UiO-66-NH$_2$ shows a bimodal distribution with mean pore diameters of 2.9 and 4.6 µm.

On the other hand, PVDF-HFP NIPS membranes accumulate most of their free space volume within the pores with a 0.25 µm diameter. The inclusion of UiO-66-NH$_2$ and MIL-125 MOFs does not alter this distribution. However, when MOF-808 is integrated within the PVDF-HFP, a bimodal distribution (d = 0.21 and 0.45 µm) is found for the composite. It is important to note that although most of the free-pore volume in the membranes is ascribed to the pore diameters described above, this does not preclude the existence of specific porosity related to macro and meso-pores below and above the main diameter value obtained from the mercury porosimetry measurements.

2.3. Nano-Structuration of PVDF-HFP@MOF Composites

The nanoscale structure variations of the PVDF-HFP membranes and of the three PVDF-HFP@MOF composites (i.e.,
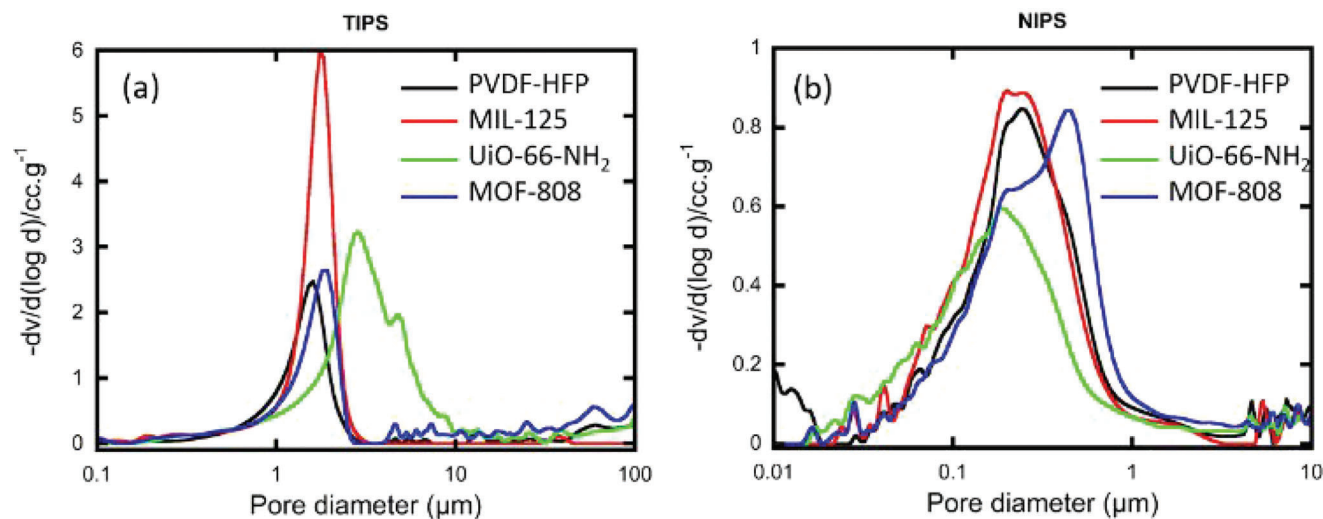
2300424 (5 of 13)

Figure 4. Cumulative pore volume dependence of the pore size for PVDF-HFP polymer membrane and composites with MOFs addition.

UiO-66-NH$_2$, MIL-125 and MOF-808) processed via TIPS and NIPS were studied by means of SANS and SAXS measurements.

Small-angle scattering is applied to characterize all types of materials at the nanometre scale in a typical interval of 1–200 nm.[52] This operational window gives access to a size-scale regime below the macro to micrometre ones observed by SEM or mercury porosimetry. In general, four SANS and SAXS features can be observed in the experimental data plotted in Figure 5: i) the scattering arising from the nano-inhomogeneities generated within the membranes due to the phase/domain structuration of the polymer itself (characteristic size ≈2–3 nm); ii) the interparticle space created due to the MOF particles agglomeration within the polymer (characteristic size ≈10–20 nm); iii) the power law decay of the scattering data that is related to the aggregates with mass or surface fractal structures in the composites; and iv) the diffraction peak in the large q region due to the crystal structure of the MOF (similar peak was observed in our recent study of separators based on polymer composites with MOFs for battery[36]). All these heterogeneities can be fitted if a proper model is applied (more information can be found in the Section S2.2, Supporting Information).

Experimental SANS and SAXS curves for the studied PVDF-HFP@MOF composites are presented in Figure 5. In addition, power law exponent, P, and radius of gyration, R_g, values obtained from the fittings of the SAXS/SANS data have been summarized in Table S2 (Supporting Information). In general terms, the data obtained for all the membranes is the typical one found in polydisperse systems forming a fractal-like aggregated structure.[53] Therefore, the differences arising from the fractal structure will be discussed, followed by a discussion of the nano-inhomogeneities detected in the different composite membranes.

PVDF-HFP membranes processed by TIPS and NIPS show similar nanostructures, with surface fractals of P = 3.8–3.9 obtained for both SANS and SAXS measurements. We attribute this fractal-structuration to the surface and/or internal organization of the PVDF-HFP around the pore structure of the membranes. The arrangement of the pore-space could be replicated in a frac-

tal manner from the macro to the mesopores observed in the porosimetry measurements and illustrated in the Figure **6** and Figure S4 (Supporting Information). That is, large pores within the PVDF-HFP matrix are interconnected by channels to mid-size pores, and mid-size pores are interconnected at the same time with small pores, giving rise to a surface fractal with an interconnected structure (Figure **6**).

When MOF particles are introduced into the PVDF-HFP matrix, the nanometric differences observed between the membranes processed by the NIPS and TIPS methods increase and similar observation was obtained for macropores according to SEM and porosimetry experiments. TIPS composites show different fractal structures depending on the MOF. For instance, bare PVDF-HFP and PVDF-HFP@UiO-66-NH$_2$ show surface fractals of P = 3.9 (Ds = 2.1) and P = 3.7 (Ds = 2.3), respectively. Its homologue MIL-125 composite also exhibits a surface fractal, but with a P = 3.3 (Ds = 2.7), indicating a higher surface roughness. Altogether, it is evidenced that the surface fractals arising from the empty pore-space of the TIPS PVDF-HFP membranes are partially modulated when MOF particles are included within the system. Therefore, this modulation gives rise to different P values when fitting the power-law decay of the SANS and SAXS data of the composites, as illustrated in Figure 6. The PVDF-HFP@MOF-808 membrane shows the most complex fractal structure. The SANS spectrum shows a mass fractal of Dm = 2.8, corresponding to dense agglomerations within the polymeric matrix. However, SAXS data reveals two types of behavior: a mass fractal with Dm = 1.7, and a surface fractal of P = 3.5 (Ds = 2.5). Overall, the SANS and SAXS data indicate a branched and interconnected fractal structure formed from anisotropic elongated pores observed by SEM. The surface-fractal structuration of PVDF-HFP@MOF-808 can be explained by the decoration of the surface of the pore space in the PVDF-HFP with MOF-808 nanoparticles. In addition, the values of the mass fractals can be closely related to the entrapment of MOF agglomerates into some of the PVDF-HFP pores.

Contrary to TIPS, NIPS composite membranes exhibit power laws with mass fractals of P = 3.7, similar to the bare PVDF-HFP
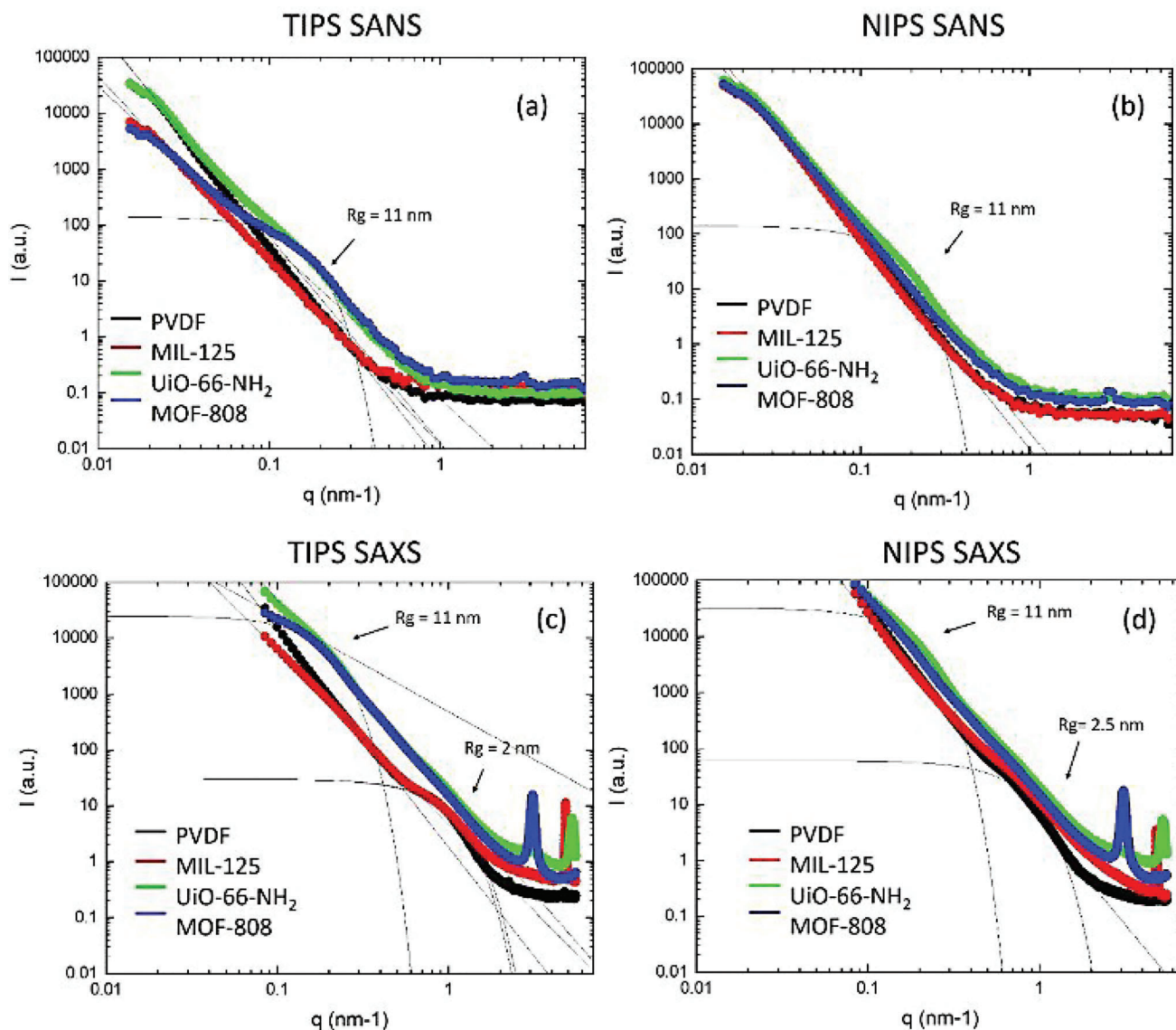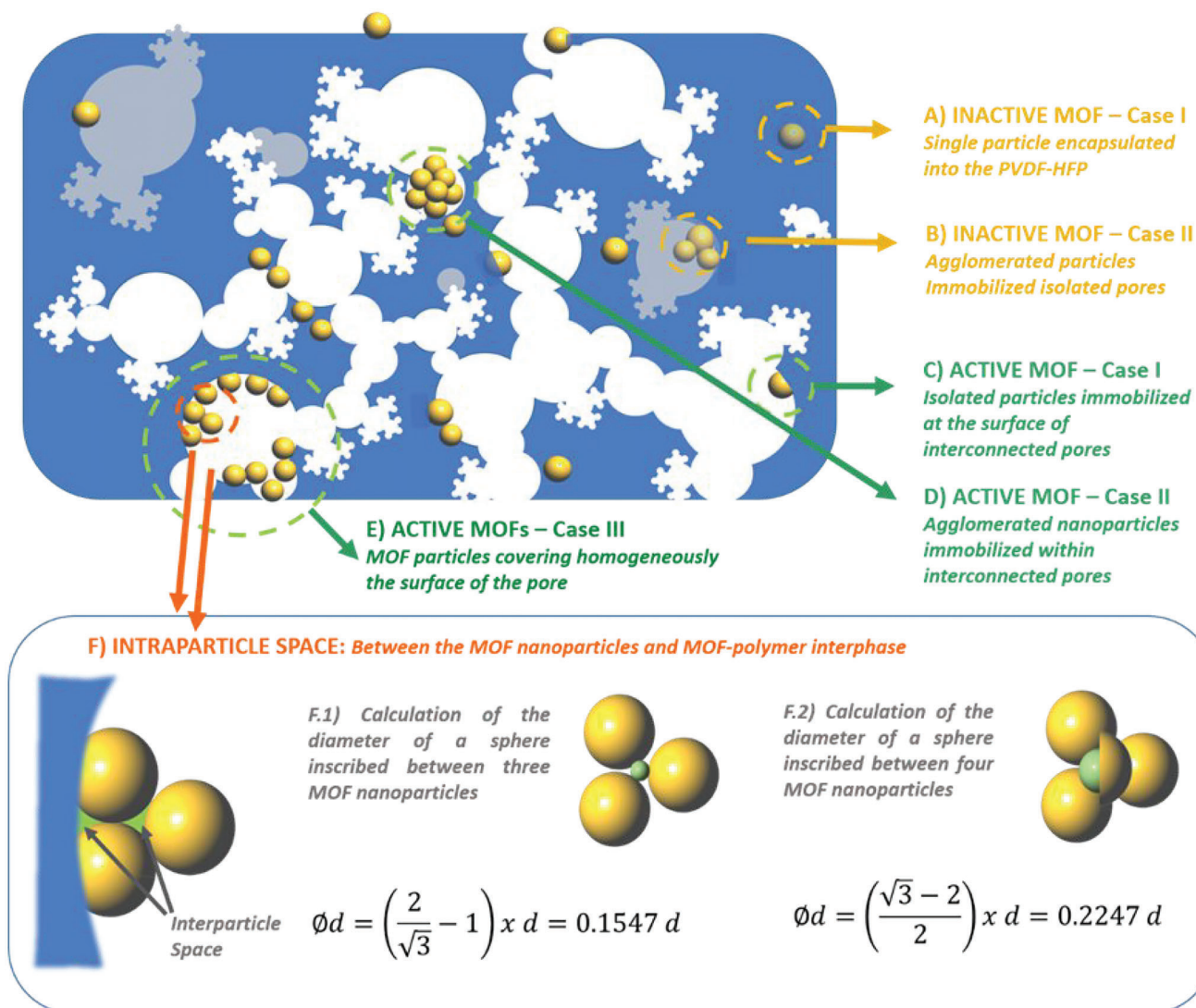
**ADVANCED
SCIENCE NEWS**

www.advancedsciencenews.com

**ADVANCED
MATERIALS
INTERFACES**

www.advmatinterfaces.de

Figure 5. SANS data for a) TIPS and b) NIPS membranes. SAXS data for c) TIPS and d) NIPS membranes.

membranes. Therefore, the nanostructuration of the polymeric matrix remains largely unaffected by the inclusion of MOF particles.
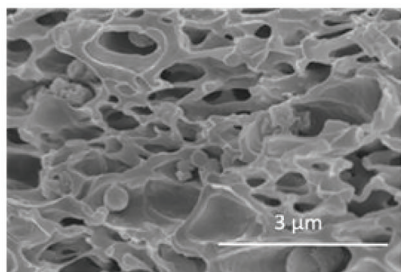
Considering the information from the SEM images and the one obtained by SANS and SAXS, the shape of the branched fractal structuration of the pores in PVDF-HFP membranes are summarized as schematized in Figure 6. In this simplified model, it can be found MOF nanoparticles finely decorating the pore space of the PVDF-HFP, as in the case of MOF-808 TIPS membrane, agglomerated MOF nanoparticles, and even single nanoparticles encapsulated within the PVDF-HFP matrix.

It is worth noting that the SANS data does not provide information about the inhomogeneities of bare polymeric membranes usually observed at higher q values using SAXS (R_g values of 2 and 2.5 nm for TIPS and NIPS membranes, respectively). We have ascribed these inhomogeneities to the PVDF-HFP perfluorinated chain arrangements at the amorphous and crystalline domains of the different phases of the polymeric matrix. For instance, a domain size between 2 and 2.5 nm would correspond to a polymeric chain of $\approx$20–22 carbons, which is much below the molecular weight of the polymer. When the MOFs are incorporated into the membrane, these inhomogeneities observed for the bare PVDF-HFP seem to disappear, with the exception of MIL-125-based composites. It is not an easy task to directly relate the small-angle scattering signal with a specific feature of the polymeric chain structuration at the nanoscale. Still, given the inhomogeneity size, it can be inferred that MOF-808 and UiO-66-NH$_2$ can alter the crystalline and amorphous domain structuration of the PVDF-HFP. It is known that including nano-objects within a PVDF-HFP matrix can significantly alter its crystallization process toward specific polymeric phases. A clear indication of this phenomenon is given by XRD, where the width of the diffraction peak from a pure polymer matrix changes with and without the presence of nano-objects.

A) INACTIVE MOF – Case I
Single particle encapsulated into the PVDF-HFP

B) INACTIVE MOF – Case II
Agglomerated particles Immobilized isolated pores

C) ACTIVE MOF – Case I
Isolated particles immobilized at the surface of interconnected pores

D) ACTIVE MOF – Case II
Agglomerated nanoparticles immobilized within interconnected pores

E) ACTIVE MOFs – Case III
MOF particles covering homogeneously the surface of the pore

F) INTRAPARTICLE SPACE: *Between the MOF nanoparticles and MOF-polymer interphase*

F.1) *Calculation of the diameter of a sphere inscribed between three MOF nanoparticles*

Interparticle Space

$$\emptyset d = \left(\frac{2}{\sqrt{3}} - 1\right) x\, d = 0.1547\, d$$

F.2) *Calculation of the diameter of a sphere inscribed between four MOF nanoparticles*

$$\emptyset d = \left(\frac{\sqrt{3} - 2}{2}\right) x\, d = 0.2247\, d$$

Single MOF particles at the PVDF-HFP matrix (case C)

3 µm

Agglomerated MOF particles at the PVDF-HFP matrix (case D)

10 µm
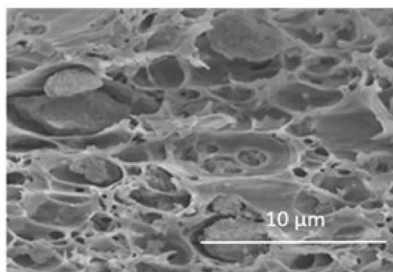
Surface decoration of the PVDF-HFP pore with MOF (case E)
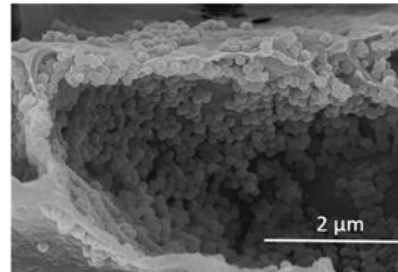
2 µm

Figure 6. Schematic representation of the overall structuration of PVDF-HFP@MOF composites. a–e) Schematic illustration of the fractal pores interconnected structure of the PVDF-HFP matrix, the MOF immobilization possibilities within the membrane, and f) the mathematic description of the interparticle space between MOF particles and at the polymer-MOF interphase. Bottom of the figure: SEM images of the different cases.

Further, additional inhomogeneities with an *Rg* value of 11 nm are found in both SANS and SAXS data for the TIPS samples containing MOF-808 and UiO-66-NH$_2$, but not for MIL-125. According to this size, they may be related to the interparticle space created by the MOF nanoparticles when they are agglomerated within the membrane since the inhomogeneity is too small to be related to the MOF nanoparticles themselves. Indeed, in a perfect packing of MOF spherical particles, the diameter of the spheres enclosed within MOF particles can be calculated by applying the equations summarized in Figure 6e. Therefore, MOF particles with diameters ranging from 50 to 200 nm generate interparticle inhomogeneities ranging from 7.8 to 31 nm, and from 11 to 45 nm, resulting from the interparticle space enclosed within a triangle or a tetrahedron of MOF particles, respectively. It is important to note that, as the packing of the MOF particles into the membrane is foreseen to deviate from the ideal case, the interparticle size could significantly vary between the minimum (7 nm) and maximum (44 nm) values. Even though the experimental evidence point toward this direction, inhomogeneities with an *Rg* value close to 11 nm are only appreciable in UiO-66-NH$_2$ and MOF-808-based samples. In both cases, the diameter of the MOF particles is 50 nm and of 100–200 nm for UiO-66-NH$_2$ and MOF-808, respectively. This hypothesis is further confirmed by the lack of this nanometer range inhomogeneity in MIL-125-based membranes because the large particle diameter of the MOF ($\approx$500 nm) would give rise to an interparticle pore space of 110 nm. This range of size is above the usual limits studied by SAXS.

On the other hand, NIPS membranes barely show the inhomogeneities corresponding to the interparticle space that we could observe in TIPS membranes, except for the UiO-66-NH$_2$-based one (Rg $\sim$12 nm). These results, together with the information obtained from SEM images (Figure 3; Figure S3, Supporting Information), point out that the interparticle space generated because of the agglomeration of MOF particles is significantly smaller in NIPS membranes. Overall, the experimental data point toward a higher percentage of isolated MOF particles stabilized at the surface or the inner body of the NIPS-type membranes. In the latter case, the MOF may be inaccessible to act as an adsorption point of the membrane. Additional SANS measurements were performed after wetting the samples with d-methanol to increase the neutron scattering contrast between the interconnected porosity and the isolated nano-inhomogeneities of the PVDF-HFP@MOF systems (Figure S5, Therefore, the nanostructuration of the po). In general terms, the power law related to the fractal structure of the membranes is not altered after wetting by deuterated solvent, but there is a general decrease in the scattering signal. In parallel, the wetting by deuterated solvent of these composite membranes showing inhomogeneities related to the MOF interparticle space induces the disappearance of this signal (Figure S5e–h, Supporting Information). This variation is attributed to the decrease of the neutron scattering contrast between the MOF and the interparticle space when the system is in contact with d-solvent. In fact, both MOF-08 and UiO-66-NH$_2$ have a scattering length density (SLD) of $\approx$2.7·10^{10} cm^{-2}, and the SLD of the air is 0. Consequently, the contrast between the two objects in an air-filled membrane is 2.7·10^{10} cm^{-2}. However, when the composite is wetted with d-methanol, the SLD of the MOF with d-methanol in its pores increases to 3.32·10^{10} cm^{-2} (considering that the porosity of the MOF is 38% in volume frac-

tion) while the SLD of the d-methanol located at the MOF interparticle space is of 5.16·10^{10} cm^{-2}. Overall, a contrast of 1.84·10^{10} cm^{-2} is obtained, a value two-fold smaller than the initial one for the as-synthesized composites.

Finally, it is important to note that a new inhomogeneity appears in all TIPS membranes after their wetting with d-methanol, except in the composite containing MIL-125. This heterogeneity has an approximate size of 2–3 nm. It has en tentatively ascribed to an increase of contrast due to the preferential uptake of d-methanol by some of the phases or amorphous/crystalline domains of the PVDF-HFP matrix. Although this initial hypothesis needs further experimentation to be corroborated, several processes, such as ionic diffusion, can be favored in the amorphous domains' regions of the PVDF-HFP. In parallel, a 2–3 nm inhomogeneity cannot be ascribed to the MOF particles (their size > 50 nm), nor to the MOF-MOF and MOF-polymer interphase.

Finally, we have focused on the NIPS PVDF-HFP@MOF-808 system to study: i) if the MOF loading alters the nanostructure of the membranes; ii) if the functionalization of the MOF-808 with cysteine before and after its incorporation into the PVDF-HFP matrix can alter somehow the nanostructuration of the polymer; and iii) if the adsorption of Cr^{VI} generates new inhomogeneities into the composites. Regarding the MOF-loading, its increase from 10 to 30 wt% induces a slight variation of the fractal structure as derived from the decrease of the P value from 3.9 in pure PVDF-HFP to 3.8 and 3.5 in composites with a 10 and 30% wt. of MOF particles (Figure S6a,b, Supporting Information). In addition, the MOF-loading induces the disappearance of the 2.5 nm size inhomogeneity ascribed to the phase or crystalline/amorphous domains of the PVDF-HFP matrix. This evidence is not unexpected since the inclusion of fillers as MOF into the PVDF-HFP matrix is known to alter its crystallinity and its crystallization as specific phases significantly.[54–57] On the other hand, the pre or post-synthetic functionalization of the MOF-808 before and after its integration in the membrane does not alter its nano structuration (Figure S6c,d, Supporting Information). More interestingly, the SANS curves remain unaltered after Cr^{VI} adsorption by the membranes, so the metal loading does not enhance the nano-inhomogeneities already present in the system (Figure S6e,f, Supporting Information).

2.4. Metal Adsorption Assessment to Evaluate the MOF Particles Encapsulation

Although the macro to nanometric structuration of the composites has been studied in the previous sections, this information is not enough to elucidate if the MOF nanoparticles incorporated into the membrane have direct contact with heavy metals in a water solution or if they are encapsulated within the polymer. To this end, we have performed metal-ion adsorption experiments on the MOF materials and the composites (Figure 7). Two different cases were investigated: the adsorption of anionic Cr^{VI} by non-functionalized PVDF-HFP@MOF membranes (Figure 7a) and the capacity to capture cationic Hg^{II} of cysteine functionalized TIPS PVDF-HFP@MOF-808 composite (Figure 7b).

First, it is important to note that PVDF-HFP lacks any capacity to adsorb Cr^{VI} or Hg^{II}. Thus, the overall adsorption capacity of the membranes arises from the MOF particles that are not
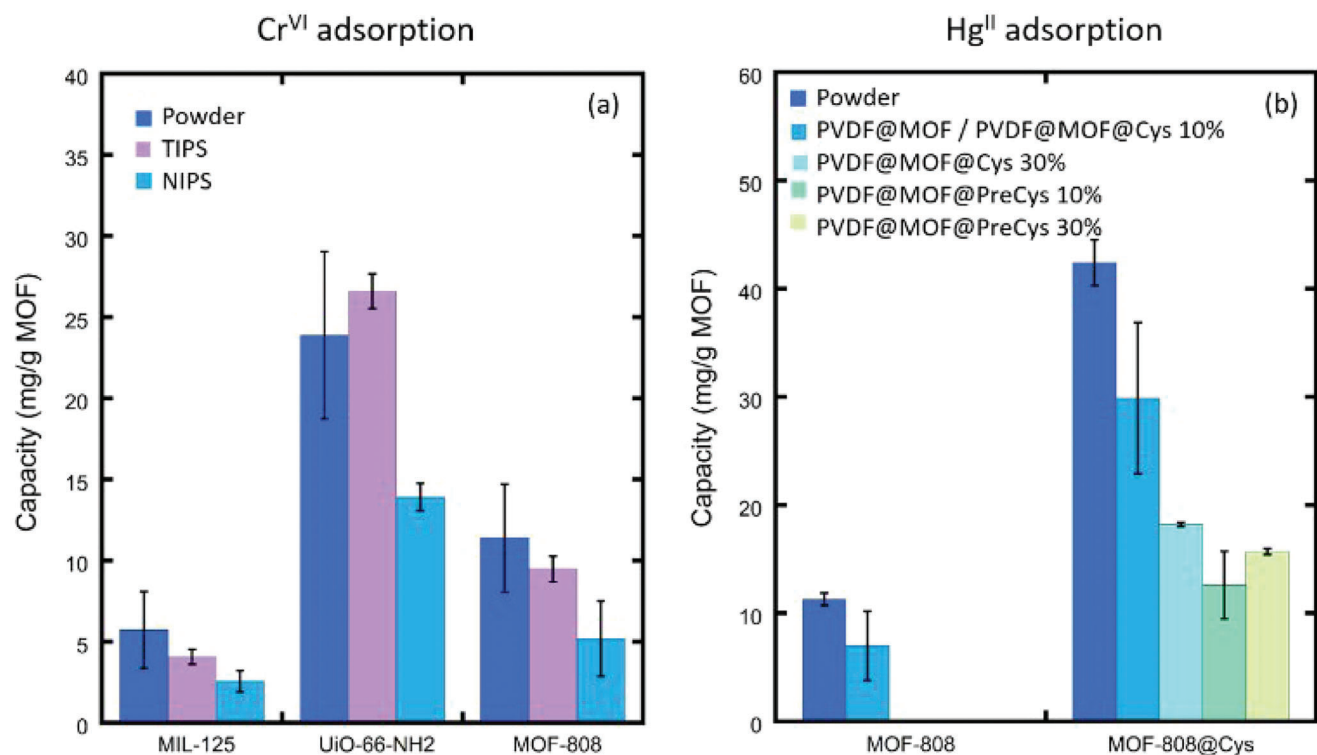
**ADVANCED
SCIENCE NEWS**

www.advancedsciencenews.com

**ADVANCED
MATERIALS
INTERFACES**
Open Access

www.advmatinterfaces.de

Figure 7. a) Cr^{VI} adsorption experiments for TIPS and NIPS membranes and b) Hg^{II} adsorption experiments for NIPS membranes with and without cysteine functionalization.

encapsulated within the polymer. Therefore, by comparing the adsorption capacity of the free MOFs and the MOFs immobilized within the membranes, the accessibility degree of the later ones can be calculated.

Regarding the Cr^{VI} capture of the studied MOFs, UiO-66-NH$_2$ shows the highest Cr^{VI} adsorption capacity (23.88 mg·g^{-1}) thanks to its linker-defective sites and the fact that amino groups welcome the capture of chromate species. MOF-808 shows an adsorption capacity for Cr^{VI} of 11.3 mg·g^{-1} ascribed to replacing the formate modulators linked to the zirconium clusters by chromate oxyanions. Finally, MIL-125 shows the smallest adsorption capacity, of 5.73 mg·g^{-1}, tentatively ascribed to a weak hydrogen interactions-driven capture.

The MOFs immobilized into TIPS membranes show similar adsorption capacities over Cr^{VI} compared to their corresponding powdered samples. The ratio between the capacity of the MOF in the membrane and the capacity of the powdered MOF allows for estimating accessibility between 80–100% of the MOF particles in the polymer. Contrary to this, MOFs immobilized within NIPS membranes show only 45 to 55% of the capacity of the powdered samples. In perspective, the small porosity shown by the surface of the NIPS membrane hinders the mobility of the chromate ions while at the same time isolates some of the MOF particles from the media. Their encapsulation degree is also related to the nanostructuration observed by SANS and SAXS, since the membranes that lack the inhomogeneities come from the agglomeration of the MOF particles and MOF-polymer interphase space are the ones that show higher ratios of MOF encapsulation within the polymer.

At this point, it has been proven that the in situ functionalization of the MOF-808 immobilized within the membrane with cysteine via water based SALI protocols is feasible. As previously reported by A. Valverde et al.[58] incorporating cysteine functions with —SH groups into the MOF-808 pore space strongly shifts its adsorption affinity to capture soft metal ions as Hg^{II}. Indeed, as explained in the cited work, the immobilization of different amino acids into the pore space of MOF-808 endows the material of metal-complexing mechanisms where single or cooperative metal-binding modes five rise to the stabilization of isolated, clustered and even partially reduced species for some specific metals.

In parallel, the cysteine encoding of powdered MOF-808 particles has been performed for comparison. We have selected PVDF-HFP@MOF-808 NIPS membrane for this study because it shows a higher degree of encapsulation of the MOF-808 particles compared to its TIPS homologue. So, it will allow to evaluate if there is any unblocking of the MOFs encapsulated within the membrane during the in situ functionalization of the system with cysteine. In parallel, this study explores as well if the encapsulation is reduced when the MOF particles are functionalized with cysteine before their incorporation into the membrane.

First, as revealed by ^{1}H-NMR, the SALI process in MOF-808 gives rise to an average functionalization of 1.7 cysteines per zirconium cluster, while 0.9 cysteines per cluster are incorporated into the MOF-808 immobilized within the membrane. That is, only 53% of the MOF-808 within the membrane is accessible to SALI, a value that is similar to the 60% accessibility obtained from the Cr^{VI} adsorption experiments. Therefore, as expected,

the SALI process does not de-block the access to the MOF encapsulated within the polymer.

Regarding the Hg^{II} adsorption performance (Figure 7b), first, an adsorption study of MOF-808 and MOF-808@Cys was performed to determine their capacity to capture Hg^{II} in the applied experimental conditions (MOF-808 = 11.3 $mg \cdot g^{-1}$ and MOF-808@Cys = 42.4 $mg \cdot g^{-1}$).

Regarding the polymeric composites, the NIPS PVDF-HPF membrane shows negligible adsorption capacity toward Hg^{II}. When non-functionalized MOF-808 is introduced in the membrane, the PVDF-HFP@MOF-808 NIPS membrane rises its capacity up to 7 $mg \cdot g_{MOF}^{-1}$. According to the Hg^{II} adsorption capacity of the bare MOF, this means accessibility of a 62% to the MOF integrated within the membrane. Similarly, the adsorption capacities over Hg^{II} of the composites functionalized with cysteine directly in the NIPS membrane (Figure 7b) point toward a 70% accessibility degree of the MOF in the 10% loaded membrane. This accessibility decays to 43% for 30% wt. MOF-808 loaded membrane that has been functionalized within cysteine molecules. Thus, increasing the MOF loading increases as well the encapsulation degree of the MOF. This issue is not solved if MOF-808 is pre-functionalized before its inclusion into the PVDF-HFP (denoted as PVDF@MOF@PreCys in Figure 7b) since both 10% and 30% wt. loaded PVDF-HFP membranes show accessibilities close to 35%, much lower than the ones reported for the in situ modified composites.

3. Conclusion

The combined and complementary experimental characterization protocols that have been applied to this study have opened the room to understand the structuration of the PVDF-HFP@MOF membranes produced by TIPS and NIPS from macro to nanometric points of view.

First, it is clear that MOF particles alter the NIPS and TIPS phase inversion process of PVDF-HFP, affecting the final pore structure of the composites. In addition, the surface and mass fractal pore nanostructure of the PVDF-HFP is as well altered when MOFs are included within the system, indicating a rougher surface in the pores wall due to the installation of the particles. Indeed, SANS and SAXS exhibit additional features related to the arrangement of MOF particles within the polymeric system. Comparative metal-ions adsorption experiments have allowed estimating the accessibility degree of the MOF particles incorporated into the membranes. The membrane's processing and the MOF's nature modulate the encapsulation degree of the particles in the polymeric system indicating an almost 100% accessibility in membranes processed by TIPS and a nearly 60% of accessibility of the particles in the membranes processed by NIPS. Although the accessibility of MOF particles in the membrane cannot be directly linked to a specific feature at the nano-scale, the TIPS membranes exhibit a more intense signal at the inhomogeneity related with the Rg of 11 Å than the NIPS ones. So, probably a certain degree of agglomeration can be beneficial, as it seems to be a consequence of a lower encapsulation of the MOF particles within the polymeric matrix. For instance, the encapsulation degree governs these MOF fractions that are accessible to be in situ modified by SALI in the membrane. It is important to note that, as far as we know, this is the first time that a SALI

direct functionalization of a polymeric-MOF composite has been performed and that this strategy has been fully effective in modulating the adsorption affinity of the system toward soft acid metal ions such as Hg^{II}.

In situ modification of polymer-MOF systems opens the perspective to improve the processing of the composites until the proper accessibility, porosity, permeability and MOF-loading features are achieved, and later on, modify the inner chemistry of the system to tailor-adapt it to the capture or separation of specific metal ions, introducing different functionalities depending on the targeted metal ion for removal.

4. Experimental Section

Composite Membranes Preparation and Characterization: PVDF-HFP@MOF membranes were prepared through two different phase inversion methods: thermal-induced phase separation (TIPS) and non-solvent-induced phase separation (NIPS), as detailed in the Supporting Information file.[24] Three different MOFs (*i.e.*, MOF-808,[59] UiO-66-NH$_2$,[12] and MIL-125[60]) were employed to prepare the composite membranes. The synthesis of the three materials was performed as detailed previously by A. Valverde and P.G- Saiz,[12,13,61,62] and the description can be also found as Supporting Information. For the functionalization of the PVDF-HFP@MOF-808 membranes with cysteine, the procedure was similar to the one applied for the MOF-808 particles functionalization reported in.[58] Hundred milligram membrane was immersed in 100 mL of a 0.05 M cysteine solution and heated at 60 °C for 24 h. Then, the membranes were washed with water twice and dried at room temperature for 24 h. The sorbent and composite membranes were fully characterized, as detailed in the Supporting Information.

The composites were then characterized through X-ray diffraction (XRD), scanning electron microscopy (SEM), thermogravimetric analysis (TGA), CO2 adsorption experiments, differential scanning calorimetry (DSC), IR spectroscopy, mercury porosimetry and small-angle neutron and X-ray scattering (SANS and SAXS respectively). Further information about the characterization conditions can be found in the Supporting Information.

Metals Adsorption Evaluation: The adsorption capacity over Cr^{VI} of the free MOFs (MIL-125, UiO-66-NH$_2$, and MOF-808) and the PVDF-HFP@MOF composites was studied employing the same ratio of MOF: metal solution for both the pristine materials and the membranes. For the adsorption experiments with MOFs, 5 mg of MOF were dispersed in 50 mL of a 5 ppm heavy metal solution and stirred overnight. Then, they were filtrated with nylon filters (0.22 μm), and the metal concentration was analyzed. For the membranes, 10 mg of the membrane was introduced in 10 mL Cr^{VI} solution at 5 ppm. The membrane was recovered after the adsorption, and the Cr^{VI} concentration of the solution was quantified. Each of these procedures was performed three times to determine the uncertainty of the described processes. Quantification of Cr^{VI} was performed through UV–Vis spectroscopy by applying the diphenyl carbazide (DPC) colorimetric methodology.[33]

In the specific case of PVDF-HFP@MOF-808, it was in situ functionalized with cysteine to study the modulation of the adsorption affinity of the MOF-808 immobilized into the polymer for cationic species as Hg^{II}. To this end, Hg^{II} adsorption experiments were performed in cysteine functionalized and non-functionalized membranes following the same procedure described for Cr^{VI} and Hg^{II}. Metal concentration was quantified by means of ICP-AES. Similarly, Cr^{VI} adsorptions were performed three times each to determine the uncertainty of the protocol.

Supporting Information

Supporting Information is available from the Wiley Online Library or from the author.

Conflict of Interest

The authors declare no conflict of interest.

Data Availability Statement

The data that support the findings of this study are available from the corresponding author upon reasonable request.

[1] J. Li, Q. Fan, Y. Wu, X. Wang, C. Chen, Z. Tang, X. Wang, *J. Mater. Chem. A* **2016**, *4*, 1737.

[2] J. Li, X. Wang, E. Power, G. Zhao, Z. Chai, C. Chen, A. Alsaedi, T. Hayat, X. Wang, *Chem. Soc. Rev.* **2018**, *47*, 2322.

[3] R. Freund, S. Canossa, S. M. Cohen, W. Yan, H. Deng, V. Guillerm, M. Eddaoudi, D. G. Madden, D. Fairen-Jimenez, H. Lyu, L. K. Macreadie, Z. Ji, Y. Zhang, B. Wang, F. Haase, C. Wöll, O. Zaremba, J. Andreo, S. Wuttke, C. S. Diercks, *Angew. Chem., Int. Ed.* **2021**, *60*, 23946.

[4] W. Schrimpf, J. Jiang, Z. Ji, P. Hirschle, D. C. Lamb, O. M. Yaghi, S. Wuttke, *Nat. Commun.* **2018**, *9*, 1647.

[5] H. Lyu, Z. Ji, S. Wuttke, O. M. Yaghi, *Chem* **2020**, *6*, 2219.

[6] S. Canossa, Z. Ji, C. Gropp, Z. Rong, E. Ploetz, S. Wuttke, O. M. Yaghi, *Nat. Rev. Mater.* **2022**, *2022*, 1.

[7] L. Oar-Arteta, T. Wezendonk, X. Sun, F. Kapteijn, J. Gascon, *Mater. Chem. Front.* **2017**, *1*, 1709.

[8] S. M. Cohen, *Chem. Rev.* **2012**, *112*, 970.

[9] J. Hao, X. Xu, H. Fei, L. Li, B. Yan, *Adv. Mater.* **2018**, *30*, 1705634.

[10] P. Deria, J. E. Mondloch, E. Tylianakis, P. Ghosh, W. Bury, R. Q. Snurr, J. T. Hupp, O. K. Farha, *J. Am. Chem. Soc.* **2013**, *135*, 16801.

[11] B. Moulin, F. Salles, S. Bourrelly, P. L. Llewellyn, T. Devic, P. Horcajada, C. Serre, G. Clet, J. C. Lavalley, M. Daturi, G. Maurin, A. Vimont, *Microporous Mesoporous Mater.* **2014**, *195*, 197.

[12] P. G. Saiz, A. Valverde, B. Gonzalez-Navarrete, M. Rosales, Y. M. Quintero, A. Fidalgo-Marijuan, J. Orive, A. Reizabal, E. S. Larrea, M. I. Arriortua, S. Lanceros-Méndez, A. García, R. Fernández de Luis, *Catalysts* **2021**, *11*, 51.

[13] P. G. Saiz, N. Iglesias, B. Gonzalez-Navarrete, M. Rosales, Y. M. Quintero, A. Reizabal, J. Orive, A. Fidalgo-Marijuan, S. Lanceros-Mendez, M. I. Arriortua, R. Fernandez de Luis, *Chemistry* **2020**, *26*, 13861.

[14] Y. Peng, H. Huang, Y. Zhang, C. Kang, S. Chen, L. Song, D. Liu, C. Zhong, *Nat. Commun.* **2018**, *9*, 187.

[15] H. Salazar, P. M. Martins, B. Santos, M. M. Fernandes, A. Reizabal, V. Sebastián, G. Botelho, C. J. Tavares, J. L. Vilas-Vilela, S. Lanceros-Mendez, *Chemosphere* **2020**, *250*, 126299.

[16] M. Grandcolas, A. Lind, *Mater. Lett.* **2022**, *307*, 131044.

[17] P. M. Martins, J. M. Ribeiro, S. Teixeira, D. Y. Petrovykh, G. Cuniberti, L. Pereira, S. Lanceros-Méndez, *Materials* **2019**, *12*, 1649.

[18] L. Y. Ng, A. W. Mohammad, C. P. Leo, N. Hilal, *Desalination* **2013**, *308*, 15.

[19] H. Salazar, J. Nunes-Pereira, D. M. Correia, V. F. Cardoso, R. Gonçalves, P. M. Martins, S. Ferdov, M. D. Martins, G. Botelho, S. Lanceros-Méndez, *Mater. Chem. Phys.* **2016**, *183*, 430.

[20] K. Vinothkumar, M. Shivanna Jyothi, C. Lavanya, M. Sakar, S. Valiyaveettil, R. G. Balakrishna, *Chem. Eng. J.* **2022**, *428*, 132561.

[21] F. Ahmadijokani, H. Molavi, A. Bahi, R. Fernández, P. Alaee, S. Wu, S. Wuttke, F. Ko, M. Arjmand, *Adv. Funct. Mater.* **2022**, *32*, 2207123.

[22] H. Choi, A. Zakersalehi, S. R. Al-Abed, C. Han, D. D. Dionysiou, in *Nanotechnology Applications for Clean Water*, 2nd ed., William Andrew Publishing, New York **2014**, pp. 123–132.

[23] K. Gupta, P. Joshi, R. Gusain, O. P. Khatri, *Coord. Chem. Rev.* **2021**, *445*, 214100.

[24] C. Ribeiro, C. M. Costa, D. M. Correia, J. Nunes-Pereira, J. Oliveira, P. Martins, R. Gonçalves, V. F. Cardoso, S. Lanceros-Méndez, *Nat. Protoc.* **2018**, *13*, 681.

[25] S. Zhang, J. Wang, Y. Zhang, J. Ma, L. Huang, S. Yu, L. Chen, G. Song, M. Qiu, X. Wang, *Environ. Pollut.* **2021**, *291*, 118076.

[26] S. Fu, L. L. Zuo, P. S. Zhou, X. J. Liu, Q. Ma, M. J. Chen, J. P. Yue, X. W. Wu, Q. Deng, *Mater. Chem. Front.* **2021**, *5*, 5211.

[27] D. Hou, J. Wang, D. Qu, Z. Luan, X. Ren, *Sep. Purif. Technol.* **2009**, *69*, 78.

[28] H. Fan, Y. Peng, *Chem. Eng. Sci.* **2012**, *79*, 94.

[29] R. J. da Silva, L. C. Mojica-Sánchez, F. D. S. Gorza, G. C. Pedro, B. G. Maciel, G. P. Ratkovski, H. D. da Rocha, K. T. O. do Nascimento, J. C. Medina-Llamas, A. E. Chávez-Guajardo, J. J. Alcaraz-Espinoza, C. P. de Melo, *J. Environ. Sci. (China)* **2021**, *100*, 62.

[30] S. Zhao, Z. Tao, L. Chen, M. Han, B. Zhao, X. Tian, L. Wang, F. Meng, *Front. Environ. Sci. Eng.* **2021**, *15*, 63.

[31] S. Bahrami, M. R. Yaftian, P. Najvak, L. Dolatyari, H. Shayani-Jam, S. D. Kolev, *Sep. Purif. Technol.* **2020**, *250*, 117251.

[32] H. Salazar, P. M. Martins, A. Valverde, R. Fernández De Luis, J. L. Vilas-Vilela, S. Ferdov, G. Botelho, S. Lanceros-Mendez, *Adv. Mater. Interfaces* **2021**, *9*, 2101419.

[33] J. M. Queirós, H. Salazar, A. Valverde, G. Botelho, R. Fernández de Luis, J. Teixeira, P. M. Martins, S. Lanceros-Mendez, *Chemosphere* **2022**, *307*, 135922.

[34] B. S. Lalia, V. Kochkodan, R. Hashaikeh, N. Hilal, *Desalination* **2013**, *326*, 77.

[35] V. F. Cardoso, C. M. Costa, D. M. Correia, E. O. Carvalho, N. Perinka, P. M. Martins, R. M. Meira, T. Marques-Almeida, T. Rodrigues-Marinho, S. Lanceros-Mendez, in *Organic Ferroelectric Materials and Applications*, (Ed: K. Asadi), Woodhead Publishing, Cambridge **2022**, pp. 375–439.

[36] J. C. Barbosa, R. Gonçalves, A. Valverde, P. M. Martins, V. I. Petrenko, M. Márton, A. Fidalgo-Marijuan, R. Fernández de Luis, C. M. Costa, S. Lanceros-Méndez, *Chem. Eng. J.* **2022**, *443*, 136329.

[37] V. I. Petrenko, L. C. Fernandes, O. I. Ivankov, C. R. Tubio, M. Tariq, J. M. S. S. Esperança, D. M. Correia, S. Lanceros-Mendez, *J. Mol. Liq.* **2022**, *360*, 119385.

[38] P. Joshi, D. Kumar, in *New Polymer Nanocomposites for Environmental Remediation*, (Eds: C. M. Hussain, A. K. Mishra), Elsevier, Amsterdam **2018**, pp. 437-456.

[39] E. Saiki, Y. Nohara, H. Iwase, T. Shikata, *ACS Omega* **2022**, *7*, 22825.

[40] O. Cuscito, M. C. Clochard, S. Esnouf, N. Betz, D. Lairez, *Nucl. Instrum. Methods Phys. Res. B* **2007**, *265*, 309.

[41] A. Valverde, R. Gonçalves, M. M. Silva, S. Wuttke, A. Fidalgo-Marijuan, C. M. Costa, J. L. Vilas-Vilela, J. M. Laza, M. I. Arriortua, S. Lanceros-Méndez, R. Fernández de Luis, *ACS Appl. Energy Mater.* **2020**, *3*, 11907.

[42] J. L. Song, Z. Q. Huang, J. Mao, W. J. Chen, B. Wang, F. W. Yang, S. H. Liu, H. J. Zhang, L. P. Qiu, J. H. Chen, *Chem. Eng. J.* **2020**, *396*, 125246.

[43] G. C. Shearer, S. Chavan, S. Bordiga, S. Svelle, U. Olsbye, K. P. Lillerud, *Chem. Mater.* **2016**, *28*, 3749.

[44] S. Dai, C. Simms, I. Dovgaliuk, G. Patriarche, A. Tissot, T. N. Parac-Vogt, C. Serre, *Chem. Mater.* **2021**, *33*, 7057.

[45] P. Martins, A. C. Lopes, S. Lanceros-Mendez, *Prog. Polym. Sci.* **2014**, *39*, 683.

[46] P. G. Saiz, A. C. Lopes, S. E. Barker, R. Fernández de Luis, M. I. Arriortua, *Mater. Des.* **2018**, *155*, 325.

[47] L. Y. Madorskaya, N. N. Loginova, Y. A. Panshin, A. M. Lobanov, *Polym. Sci. U.S.S.R.* **1983**, *25*, 2490.

[48] S. Zulfiqar, M. Zulfiqar, M. Rizvi, A. Munir, I. C. McNeill, *Polym. Degrad. Stab.* **1994**, *43*, 423.

[49] C. M. Costa, M. N. T. MacHiavello, J. L. G. Ribelles, S. Lanceros-Méndez, *J. Mater. Sci.* **2013**, *48*, 3494.

[50] P. Thakur, A. Kool, B. Bagchi, S. Das, P. Nandy, *Phys. Chem. Chem. Phys.* **2015**, *17*, 1368.

[51] A. C. Lopes, I. Correia Neves, S. L. Mendez, *J. Phys. Chem. C* **2015**, *119*, 5211.

[52] T. A. Steriotis, K. L. Stefanopoulos, A. C. Mitropoulos, N. K. Kanellopoulos, *Membrane Sci. Technol.* **2000**, *6*, 1.

[53] O. v. Tomchuk, *J. Phys. Condens. Matter* **2020**, *65*, 709.

[54] F. Guo, J. Zhao, F. Li, D. Kong, H. Guo, X. Wang, H. Hu, L. Zong, J. Xu, *CrystEngComm* **2020**, *22*, 6207.

[55] S. Bodkhe, P. S. M. Rajesh, S. Kamle, V. Verma, *J. Polym. Res.* **2014**, *21*, 434.

[56] I. S. Elashmawi, *Cryst. Res. Technol.* **2007**, *42*, 389.

[57] I. S. Elashmawi, *Mater. Chem. Phys.* **2008**, *107*, 96.

[58] A. Valverde, G. I. Tovar, N. A. Rio-López, D. Torres, M. Rosales, S. Wuttke, A. Fidalgo-Marijuan, J. M. Porro, M. Jiménez-Ruiz, V. G. Sakai, A. García, J. M. Laza, J. L. Vilas-Vilela, L. Lezama, M. I. Arriortua, G. J. Copello, R. F. de Luis, *Chem. Mater.* **2022**, *34*, 9666.

[59] J. Jiang, F. Gándara, Y. B. Zhang, K. Na, O. M. Yaghi, W. G. Klemperer, *J. Am. Chem. Soc.* **2014**, *136*, 12844.

[60] H. Wang, X. Yuan, Y. Wu, G. Zeng, X. Chen, L. Leng, Z. Wu, L. Jiang, H. Li, *J. Hazard. Mater.* **2015**, *286*, 187.

[61] A. Valverde, D. Payno, L. Lezama, J. M. Laza, S. Wuttke, R. Fernández de Luis, *Adv. Sustain. Syst.* **2022**, *6*, 2200024.

[62] G. I. Tovar Jimenez, A. Valverde, C. Mendes-Felipe, S. Wuttke, A. Fidalgo-Marijuan, E. S. Larrea, L. Lezama, F. Zheng, J. Reguera, S. Lanceros-Méndez, M. I. Arriortua, G. Copello, R. F. de Luis, *ChemSusChem* **2021**, *14*, 2892.

2300424 (13 of 13)